Keratinocyte-Derived Exosomes in Painful Diabetic Neuropathy

Authors: James Coy-Dibley[1], Nirupa D. Jayaraj[1], Dongjun Ren[2], Paola Pacifico[1], Abdelhak Belmadani[1, 2], Yi-Zhi Wang[1], Kamil K. Gebis[1], Jeffrey N. Savas[1], Amy S. Paller[3], Richard J. Miller[2], Daniela M. Menichella[1, 2]^.

Author affiliation: [1]Department of Neurology, Feinberg School of Medicine, Northwestern University, Chicago, IL, USA, [2]Department of Pharmacology, Feinberg School of Medicine, Northwestern University, Chicago, IL, USA. [3]Department of Dermatology, Feinberg School of Medicine, Northwestern University, Chicago, IL, USA

^ Corresponding author: Daniela Maria Menichella

James Coy-Dibley, MFA

Conflict of interest statement: The authors have declared that no conflict of interest exists.

ABSTRACT

Painful diabetic neuropathy (PDN) is a challenging complication of diabetes with patients experiencing a painful and burning sensation in their extremities. Existing treatments provide limited relief without addressing the underlying mechanisms of the disease. PDN involves the gradual degeneration of nerve fibers in the skin. Keratinocytes, the most abundant epidermal cell type, are closely positioned to cutaneous nerve terminals, suggesting the possibility of bi-directional communication. Exosomes are small extracellular vesicles released from many cell types that mediate cell to cell communication. The role of keratinocyte-derived exosomes (KDEs) in influencing signaling between the skin and cutaneous nerve terminals and their contribution to the genesis of PDN has not been explored. In this study, we characterized KDEs in a well-established high-fat diet (HFD) mouse model of PDN using primary adult mouse keratinocyte cultures. We obtained highly enriched KDEs through size exclusion chromatography and then analyzed their molecular cargo using proteomic analysis and small RNA sequencing. We found significant differences in the protein and microRNA content of HFD KDEs compared to KDEs obtained from control mice on a regular diet (RD), including pathways involved in axon guidance and synaptic transmission. Additionally, using an *in vivo* conditional extracellular vesicle (EV) reporter mouse model, we demonstrated that epidermal-originating GFP-tagged KDEs are retrogradely trafficked into the DRG neuron cell body. Overall, our study presents a potential novel mode of communication between keratinocytes and DRG neurons in the skin, revealing a possible role for KDEs in contributing to the axonal degeneration that underlies neuropathic pain in PDN. Moreover, this study presents potential therapeutic targets in the skin for

47 developing more effective, disease-modifying, and better-tolerated topical interventions
48 for patients suffering from PDN, one of the most common and untreatable peripheral
49 neuropathies.

50 **INTRODUCTION**

51 Diabetes mellitus affects 29.3 million adults with pre-diabetes in an additional 115.9
52 million[1]. Painful diabetic neuropathy (PDN) is a disabling, intractable, and common
53 syndrome occurring in approximately 25% of diabetics[2-5]. The associated neuropathic
54 pain significantly impacts the quality of life for patients[6]. Despite the high prevalence and
55 impact, current therapies for PDN have limited effects in treating pain[7-10], fail to remediate
56 the damage to nerves, and have side effects associated with their systemic
57 administration[10-12]. Therefore, there is an urgent need for better tolerated and more
58 effective therapies for PDN.

59 PDN is characterized by neuropathic pain associated with dorsal root ganglion
60 (DRG) nociceptor hyperexcitability and the degeneration with loss or retraction of the
61 cutaneous DRG neuron axons that innervate the skin (small fiber neuropathy)[13,14]. A
62 critical barrier to developing effective treatments for PDN is the lack of understanding of
63 the molecular mechanisms leading to neuropathic pain and small fiber neuropathy.

64 Keratinocytes are the most abundant epidermal cell type. Recent studies have
65 discovered a new role for keratinocytes in mediating innocuous and noxious touch and
66 thermal sensation in healthy skin[15]. Keratinocytes detect touch stimuli in the skin and
67 transmit mechanical information related to pressure and brushing[16,17]. Optogenetic
68 inhibition of keratinocytes *in vivo* inhibits the responses to noxious mechanical and
69 thermal stimuli[17,18]. There is also evidence that keratinocytes may contribute to persistent
70 neuropathic pain. A study involving the transplantation of human keratinocytes into
71 rodents with transected nerves showed increased excitability of DRG neurons and

72 chronic pain *in vivo*[19]. However, the specific role of keratinocytes in PDN has not been
73 widely investigated.

74 The skin is a highly complex biological system. Along with nociceptive DRG
75 neurons, various other neuronal subpopulations terminate in the skin, both in the dermis
76 and the epidermis[5]. Keratinocytes are closely juxtaposed to cutaneous nerve terminals,
77 suggesting that there may be bidirectional communication. Interestingly, in rodents and
78 human skin, cutaneous nerve terminals in the epidermis form synapse-like contacts and
79 also tunnel through keratinocytes, where they form connexin 43-positive gap junctions,
80 enabling direct cellular communication[20,21]. However, the functional implications of such
81 observations remain unclear. One such ubiquitous mode of intercellular communication
82 recently garnering more appreciation in the skin is mediated by extracellular vesicles
83 (EVs).

84 Exosomes, which are small EVs composed of lipids, proteins and nucleic acids[22-
85 25], were initially posited to be involved in removing cellular waste[26]. However, a substantial
86 body of research now suggests a wider role in intercellular communication. Exosomes
87 are released from most cell types and have been linked to several neurogenerative
88 diseases[27,28] and the progression of different cancers[29]. Keratinocyte-derived exosomes
89 (KDEs) have demonstrated their ability to modulate melanocyte pigmentation[30], regulate
90 dermal fibroblast gene expression[31], mediate crosstalk with macrophages in cutaneous
91 wound healing[32], and play a crucial role in dermal immune responses in psoriasis [33,34].
92 Additionally, EVs derived from mesenchymal stem cells can directly alter the excitability
93 of DRG nociceptors in mice[35]. Exploration of the role of exosomes in diabetes, however,
94 has primarily focused on adipose tissue and inter-organ communication[36-38]. Recent

95 studies have unveiled a potential role for exosomes in impaired wound healing associated
96 with diabetes[39]. Yet, research on the effects of exosomes on diabetic neuropathy is limited
97 and has been conducted using exosomes isolated from mesenchymal[40,41] or Schwann
98 cells[42]. Notably, exosomes isolated from mesenchymal stromal cells have shown promise
99 in ameliorating peripheral neuropathy in a mouse model of diabetes[40]. Conversely,
100 exosomes derived from high glucose-stimulated Schwann cells have been found to
101 promote the development of diabetic neuropathy in mice[42]. A rigorous and comprehensive
102 investigation of keratinocyte-derived exosomes and their role in PDN represents an
103 important, yet understudied frontier in pain and peripheral neuropathy research.

104 Using size exclusion chromatography, we obtained enriched keratinocyte-derived
105 exosomes from mice and performed an unbiased molecular cargo characterization with
106 proteomics and small RNA sequencing. We found significantly altered protein and
107 microRNA content of keratinocyte-derived exosomes from high-fat diet (HFD)-induced
108 PDN compared to regular diet (RD) control mice. Altered pathways were involved in axon
109 guidance and synaptic transmission. Additionally, using an *in vivo* conditional EV reporter
110 mouse line, we demonstrated that epidermal-originating GFP-tagged keratinocyte-
111 derived exosomes are retrogradely trafficked into the DRG neuron cell body. Overall, we
112 present evidence that supports keratinocyte-derived exosomes as a novel interaction
113 pathway between epidermal keratinocytes and DRG neurons and that altered cutaneous
114 EV-trafficking may play a functional role in the development of the small fiber neuropathy
115 observed in PDN.

RESULTS

Keratinocytes release a diverse population of exosomes. To study keratinocyte-derived exosomes (KDEs), we fractionated cell-conditioned medium (CCM) from cultured adult mouse primary keratinocytes[17,18] using a qEV 35-nm size-exclusion chromatography column[43] (Figure 1A). We observed an increasing total protein concentration with each successive fraction (Figure 1B; silver stain) and immunoblotted for known exosome markers. Fractions 2 and 3 were enriched with the exosome-associated cargo markers Alix, Tsg101, and Syntenin-1 as well as the transmembrane tetraspanins CD63 and CD81[23-25,44]. These fractions were devoid of GM130 and Calnexin, which are Golgi-associated proteins[45] (Figure 1B). Thus, pooled fractions 2 and 3, representing our highly enriched KDE fractions with minimal free-floating protein contamination, were used for all subsequent analyses[46].

To investigate the role of KDEs in painful diabetic neuropathy, we employed the clinically relevant and well-established HFD model of PDN[47-50], developed by feeding mice a high fat diet for ten weeks, leading to obesity, glucose intolerance and mechanical allodynia with small-fiber degeneration[48-50]. Cultured keratinocytes from the RD and HFD mice were grown to 90% confluency in low-calcium, EV-depleted medium for scratch assays. The HFD keratinocytes had impaired wound healing during the 3 days of observation (Supplemental Figure 1A-B), consistent with what has been shown in scratch assays with high glucose exposure[51] and what is observed in diabetic patients[52]. Fraction 2/3 KDEs had sizes within the range of exosomes of 59.2 ± 14.5nm (RD; Figure 1C) and 70 ± 26.3nm (HFD; Supplemental Figure 2B) by dynamic light scattering (DLS) and concentration peaks at 95 ± 6.1nm (RD; Figure 1D) and 86 ± 8.7nm (HFD; Supplemental

139 Figure 2C) by nanoparticle tracking analysis (NTA). Tunable resistive pulse sensing
140 (TRPS) determined that the mean size average for RD KDEs were 97.7 ± 4.5nm with a
141 concentration peak of 72.3 ± 4.5nm (Figure 1E). KDEs from both RD and HFD were
142 visualized via negative staining (Figure 1F) and cryo-electron microscopy (Figure 1G),
143 which revealed the expected crescent morphology and intact vesicular structure.

144

145 **Keratinocytes release soluble factors that encourage DRG neuron axonal growth.**
146 Given that loss of cutaneous innervation is reported in PDN[13,14,49], we next sought to
147 investigate the role of KDEs on DRG axonal growth. We employed a microfluidics co-
148 culture system with primary adult mouse DRG neurons in one chamber and adult mouse
149 keratinocytes in the other (Figure 2A). This setup allowed for cell medium exchange only
150 through the microchannels between the chambers. Interestingly, we found that DRG
151 neuronal axons crossed the microchannels separating the two chambers at a higher rate
152 when grown in a co-culture with keratinocytes compared to when grown alone, indicating
153 that keratinocytes release soluble growth factors that promote axonal growth (Figure 2B-
154 C).

155 To test whether mouse KDEs are functional, we labeled them with DIR, which is a
156 carbocyanine DiOC18(7) lipophilic fluorescent dye, and added them to primary DRG
157 neuron cultures. We observed a robust uptake of these KDEs by both the cell bodies and
158 neurites of the neurons (Figure 2D). To better model physiological relevance, we then
159 cultured DRG neurons in one chamber of our microfluidic system and allowed their
160 neurites to occupy all the microchannels, thus preventing the free flow of medium
161 between chambers. We then added DIR-labeled KDEs to the empty chamber to test

162 whether they could be transported through the neurites to the DRG neuron cell body.
163 Indeed, DIR-labeled KDEs were readily detected in the DRG neuron cell bodies 16 hours
164 post application, suggesting the retrograde transport of DIR-labeled KDEs through the
165 neurites[53] (Figure 2E).

166

167 **Keratinocyte-derived exosomes alter their protein cargo in painful diabetic**
168 **neuropathy.** We characterized the KDE protein content in the context of PDN using a
169 proteomic approach[54]. The analysis was performed on the pooled fractions 2/3 using
170 liquid chromatography-tandem mass spectrometry (LC-MS/MS) for both RD and HFD
171 KDEs (Figure 3A). A gene ontology enrichment analysis on proteins detected in pooled
172 fractions 2/3 for both groups clustered in EV categories, suggesting a robust small EV
173 enrichment for both RD and HFD KDEs (Figure 3B). Importantly, we found similar
174 quantities based on the number of spectral counts of the canonical exosome-associated
175 proteins Alix, Tsg101, and Syntenin-1 in both samples (Figure 3C). Fractions 2/3-enriched
176 proteins also significantly clustered in the GO enrichment term 'Axon Development,'
177 (Figure 3C; Insert), suggesting neuron-keratinocyte communication via exosomes.
178 Moreover, we identified 90 differentially expressed exosome-associated proteins (EAPs;
179 FC ≥ 1.5, $p < 0.05$) between RD and HFD KDEs, with biological replicates clustering by
180 group (Figure 3D-E). The differentially expressed REACTOME pathway with 'MAPK
181 Family Signaling Cascades' included both Mapk1 and Mapk3 (Figure 3G left; Adjusted p-
182 value ≤ 0.05), with Mapk1 found in fraction 2/3 (Figure 3F). Furthermore, a gene ontology
183 enrichment analysis on the EAPs revealed 'Wound Healing' as differentially expressed in
184 HFD KDEs (3G middle; Adjusted p-value ≤ 0.05), consistent with the known impairment

185 in diabetic patients[55] and as shown in our 2D primary HFD keratinocyte scratch assays
186 (Supplemental Figure 1A-B). Notably, several annexins were differentially expressed, with
187 annexin VII in fraction 2/3 of our immunoblots (Figure 3F); annexins play a role in ESCRT-
188 III mediated plasma membrane repair[56-59] and wound healing[56]. Another differentially
189 expressed pathway was 'Neurotransmitter Secretion' (Figure 3G right; adjusted p-value
190 ≤ 0.05), consistent with the physical localization of DRG nerve afferents, which tunnel
191 through the keratinocyte cytoplasm to form synapse-like contacts[20,21]. Taken together,
192 these differentially expressed GO pathways support an alteration in the neuron-
193 keratinocyte communication pathways in diabetes-related PDN.

194

195 **The microRNA cargo of keratinocyte-derived exosomes is altered in painful**
196 **diabetic neuropathy.** Exosomes contain gene-modifying RNAs, with microRNAs being
197 the most abundant RNA species[43]. Several microRNAs have been associated with pain
198 in diabetic neuropathy[60], but the KDE microRNA content has not yet been identified in the
199 context of PDN. Hence, we next investigated the microRNA cargo of RD and HFD KDEs
200 using an unbiased small-library RNA sequencing approach.

201 The top ten most abundant microRNAs identified, including their variants,
202 accounted for 74.8% of the total small RNA sequenced for both groups (Figure 4A).
203 Additionally, the top two hits, the let-7 and miR-23 families, accounted for almost 40% of
204 the total RNA sequenced for both groups. By cross-referencing 3 separate databases
205 (Figure 2B), the predicted protein targets of these small RNAs were used to run a KEGG
206 enrichment analysis for let-7 and miR-23, with both revealing 'Axon Guidance' as a
207 predicted target pathway (Figure 4C). Between the RD and HFD KDEs, there were 35

208 significant differentially expressed microRNAs that clustered by group (Figure 4D) and 33
209 with a fold change (FC) ≥ 1.5 (Figure 4E). By cross-referencing the same three databases,
210 the predicted target proteins from each microRNA were run through a gene ontology
211 enrichment analysis with three producing significant target pathways (Figure 4F;
212 Supplemental Figure 3F-G). Both miR-684, which has been implicated in multiple
213 sclerosis[61], and miR24-3p, which has been studied in the context of cancers[62,63] along
214 with its regulation of proliferation related to annexin-6 activity[64], revealed predicted target
215 axon-guidance related pathways (Figure 4G), further providing compelling evidence for a
216 neuron-keratinocyte communication pathway via KDEs under both normal physiology and
217 PDN. Given that both the proteomic and small RNA sequencing datasets revealed
218 predicted target pathways involved in axon guidance and that painful diabetic neuropathy
219 is accompanied by peripheral nerve degeneration[49], we next designed an *in vivo* animal
220 model to investigate the interaction between KDEs and DRG neuron afferent fibers.
221
222 **Epidermal keratinocyte-derived exosomes are fluorescently labeled with CD63-**
223 **emGFP**. Fraction 2/3 from our keratinocyte CCM consistently immunoblotted for the
224 transmembrane tetraspanins CD63 and CD81[24] (Figure 1B), in addition to the luminal
225 exosome markers Alix, Syntenin-1, and Tsg101. We crossed the commercially available
226 CD63-emGFP fl/fl mouse line (JacksonLaboratory Strain#:036865) and crossed it with
227 K14-Cre mice to generate a K14-CD63-emGFP EV reporter mouse model (Figure 5A) to
228 label exosomes originating from basal layer keratinocytes and their progeny. We
229 observed robust GFP expression throughout the keratinocyte progeny, with K14 staining
230 co-localizing in basal layer keratinocytes, confirming the limitation of expression to the

231 epidermis (Figure 5B). Furthermore, we immunoblotted whole epidermis cell lysate and
232 detected both the membrane-bound CD63-GFP fusion protein and soluble GFP (Figure
233 5C), presumably due to endogenous protein recycling. We next cultured keratinocytes
234 from this EV-reporter mouse. As expected, we observed a strong GFP signal along the
235 outer membrane of these keratinocytes (Figure 5D). We next immunoblotted all ten
236 fractions obtained from CCM of primary keratinocyte cultures for GFP and detected a
237 strong GFP signal, both the fusion and soluble forms, in fractions 2/3, which corresponded
238 to our KDE enriched fractions (Figure 5E). Furthermore, isolated GFP-labeled KDEs were
239 functionally internalized by DRG neurons with GFP detected in both the neuron cell
240 bodies and neurites (Supplemental Figure 4A). Given the gene ontology enrichment
241 pathways highlighted from our proteomic and small RNA sequencing experiments, we
242 next sought to better understand the neuron-keratinocyte communication pathway using
243 our EV reporter mouse line.
244
245 **Epidermal keratinocyte-derived exosomes are retrogradely transported to the DRG**
246 **neuron cell bodies in male and female mice**. We further investigated the *in vivo*
247 conditional EV-reporter mouse, shifting our focus towards the DRGs. Notably, we
248 detected a GFP signal in DRG cross-sections from both RD and HFD EV-reporter mice
249 (Figure 6A; Supplemental Figure 4B) and not in WT DRG controls (Figure 6B).
250 Additionally, the cell lysate of K14-CD63-GFP (KCG) DRG neurons immunoblotted for
251 GFP (Figure 6C), further supporting the evidence for the retrograde transport of GFP-
252 positive epidermal exosomes to the DRG neuron cell bodies. We next cultured primary
253 DRG neurons from the EV-reporter mouse model for both RD and HFD. We observed

254 robust GFP expression in both groups (Figure 6D) with no GFP signal in WT controls
255 (Figure 6E). The GFP observed in these primary DRG neuron cultures presented in the
256 same punctate pattern observed in the DIR-labeled exosomes (Figure 2D) and GFP-
257 labeled exosomes applied to primary DRG cultures[46] (Supplemental Figure 4A). Indeed,
258 we detected these puncta in both the neuron cell bodies and along the neurites (Figure
259 6F). These data strongly suggest that CD63-GFP-positive keratinocyte-derived
260 exosomes are retrogradely transported from the epidermis to DRG neuron cell bodies,
261 representing a novel mode of communication.

262 **DISCUSSION**

263 We isolated and characterized keratinocyte-derived exosomes (KDEs)
264 morphologically and molecularly using an unbiased proteomic and small RNA sequencing
265 approach. Our research revealed that KDEs alter their cargo in a mouse model of painful
266 diabetic neuropathy (PDN), and we identified several gene ontology enrichment pathways
267 that were differentially expressed. In both "omic" datasets, neuron-keratinocyte pathways
268 were enriched both under normal physiology and in PDN. Additionally, we created a K14-
269 CD63-emGFP extracellular vesicle (EV)-reporter mouse line and observed a GFP signal
270 in the DRG neurons and neurites, suggesting that keratinocyte-derived GFP-tagged
271 exosomes are retrogradely trafficked from epidermal keratinocytes into the DRG neurons
272 of mice.

273 These findings suggest a direct communication pathway between the epidermis
274 and the peripheral nervous system, which is altered in our HFD mouse model of PDN. In
275 our microfluidic paradigm, the presence of keratinocytes enhanced neurite outgrowth,
276 indicating release of a soluble factor by keratinocytes that encourages neurite growth
277 (Figure 2A-C). Proteomic analysis of our KDEs revealed that they contained several
278 catenin and plexin isoforms (3C; Insert). The canonical WNT-signaling pathway plays a
279 significant role in axon development in the central[65,66] and peripheral[67] nervous systems
280 and has been implicated in Schwann cell-axon communication[68]. Plexins, the surface
281 receptors for semaphorins, are involved in neuron axonal growth and guidance, as well
282 as a host of other functions[69-72]. Semaphorin 4C-Plexin-b2 signaling has been reported
283 to be markedly increased in states of persistent pain in mice, and downregulation of this
284 pathway led to the impairment of inflammatory hypersensitivity via RhoA-ROCK-

285 dependent mechanisms[73]. Additionally, Sema3A and Plexin A were reported to be
286 dysregulated in the spinal cord of a HFD model of PDN[74]. To our knowledge, this is the
287 first report of these proteins being present as KDE cargo. Additionally, notch1, which was
288 recently reported to facilitate neuron-to-neuron communication through EVs in the
289 hippocampus of mice[46], was detected in our KDEs for all three biological replicates of
290 both diet groups (3C; Insert), suggesting that this mechanism of internalization may also
291 apply to keratinocyte-neuron terminal endings in the skin. Notch signaling is known to
292 play a prominent role in developing neurons, including in axon guidance[75,76]. Pathogenic
293 variants in the Notch ligand Jagged1 were implicated in the development of peripheral
294 neuropathy in two independent families and confirmed in a mouse model[77]. Thus, Notch
295 signaling may represent an unexplored, novel communication pathway between
296 keratinocytes and DRG neuron terminal nerve endings.

297 The KDEs from both groups contain differentially expressed synaptotagmin, which
298 is an essential component of the presynaptic vesicle release complex that facilitates
299 vesicle fusion with the plasma membrane[78,79], along with synaptophysin and synapsin-2,
300 both of which are involved in regulating vesicle docking to the inner plasma membrane[80-
301 82] (3G; Right Panel). These proteins have all been previously reported in keratinocytes[83].
302 However, it is still unclear why these proteins are present as KDE cargo and what their
303 function in keratinocyte-to-neuron communication might be. Further experiments are
304 required to validate all these cargo proteins, both in mice and human KDEs, and to
305 investigate their mechanism of action on nerve terminals.

306 Our small RNA sequencing dataset aligned with the proteomic data. The top two
307 most abundant small RNAs, let-7 and miR-23 (Figure 4A), were predicted to target

308 several prominent signaling pathways that overlapped with the proteomic dataset,
309 including MAPK signaling and the WNT signaling pathways (Figure 4C). A recent study
310 has indicated that partially inhibiting p38-MAPK activation in a diabetic neuropathy rat
311 model led to anti-hyperalgesic effects, suggesting a significant role for MAPKs in
312 nociception modulation[84]. KDEs from both our groups contained a diverse range of MAP
313 kinases (MAPKs), with mapk1 differentially expressed in our HFD model. Both let-7 and
314 miR-23 have been shown to modulate MAPK activity[85,86]. Additionally, two differentially
315 expressed microRNAs suggested altered keratinocyte-to-neuron communication (Figure
316 4F-G). An altered expression of miR-24-3p has been reported in cancer[62,63,87,88] and
317 diabetes[89]. By cross-referencing three separate databases for predicted targets and
318 running a gene ontology enrichment analysis, one predicted pathway for miR-24-3p
319 modulation is plexin-semaphorin activity, and our proteomic dataset suggested plexin-b2
320 as a cargo protein (Figure 3C). However, the precise mechanism by which these
321 microRNAs regulate axon guidance and potentially contribute to PDN remains unclear.
322 Further studies are necessary to understand how these microRNAs modulate target
323 proteins and pathways, either directly or indirectly.

324 The DRG transcriptome is substantially altered in PDN[90], resulting in
325 hyperexcitability of the nociceptive neurons that drive neuropathic pain[49,90] and presenting
326 a possible druggable system for future therapeutics. In our studies, using an EV-reporter
327 mouse line in which KDEs are labelled with CD63-emGFP (Figure 6A), we detected a
328 GFP signal in the DRG neuron cell bodies and neurites (Figure 6F). This indicates that
329 GFP-containing exosomes originating in the epidermis are retrogradely trafficked into the
330 DRG neuron cell body, where presumably they can initiate transcriptional changes due to

331 their cargo. It should be noted that the GFP species detected, at least from our
332 immunoblotting, was the non-fused form of GFP rather than the CD63-GFP fusion form
333 (Figure 6C), but that soluble GFP was also detected in the epidermis (Figure 5C) and
334 KDE fractions (Figure 5E) in high abundance. It may be that the GFP-tagged exosomes
335 are trafficked to DRG neurons, where they release their transcription-altering cargo, and
336 the fusion protein is subsequently degraded into the soluble GFP that we detected in
337 immunoblotting.

338 This study enhances our understanding of the communication between
339 keratinocytes and DRG neurons and reveals a new role for KDEs in possibly promoting
340 axonal degeneration, which underlies neuropathic pain in PDN. As many genes show
341 differential expression in DRG neurons in PDN mice compared to control mice[91], our
342 studies support a novel strategy for treating PDN by focusing on the skin rather than the
343 entire body. One of the challenges with current PDN treatments is their systemic
344 administration and off-target effects[10-12]. Here, we present evidence for a delivery
345 pathway from epidermal keratinocytes to the peripheral nervous system, which could be
346 utilized to develop and deliver improved topical treatments for PDN and other nervous
347 system diseases. Additionally, our investigation into the role of exosome-mediated
348 communication between keratinocytes and DRG neurons has broader implications.
349 Indeed, exosomes hold great promise as novel disease biomarkers, therapeutic agents,
350 and drug delivery systems. This potential extends beyond PDN, laying the groundwork
351 for exploring new avenues in pain and peripheral neuropathy research and treatment.

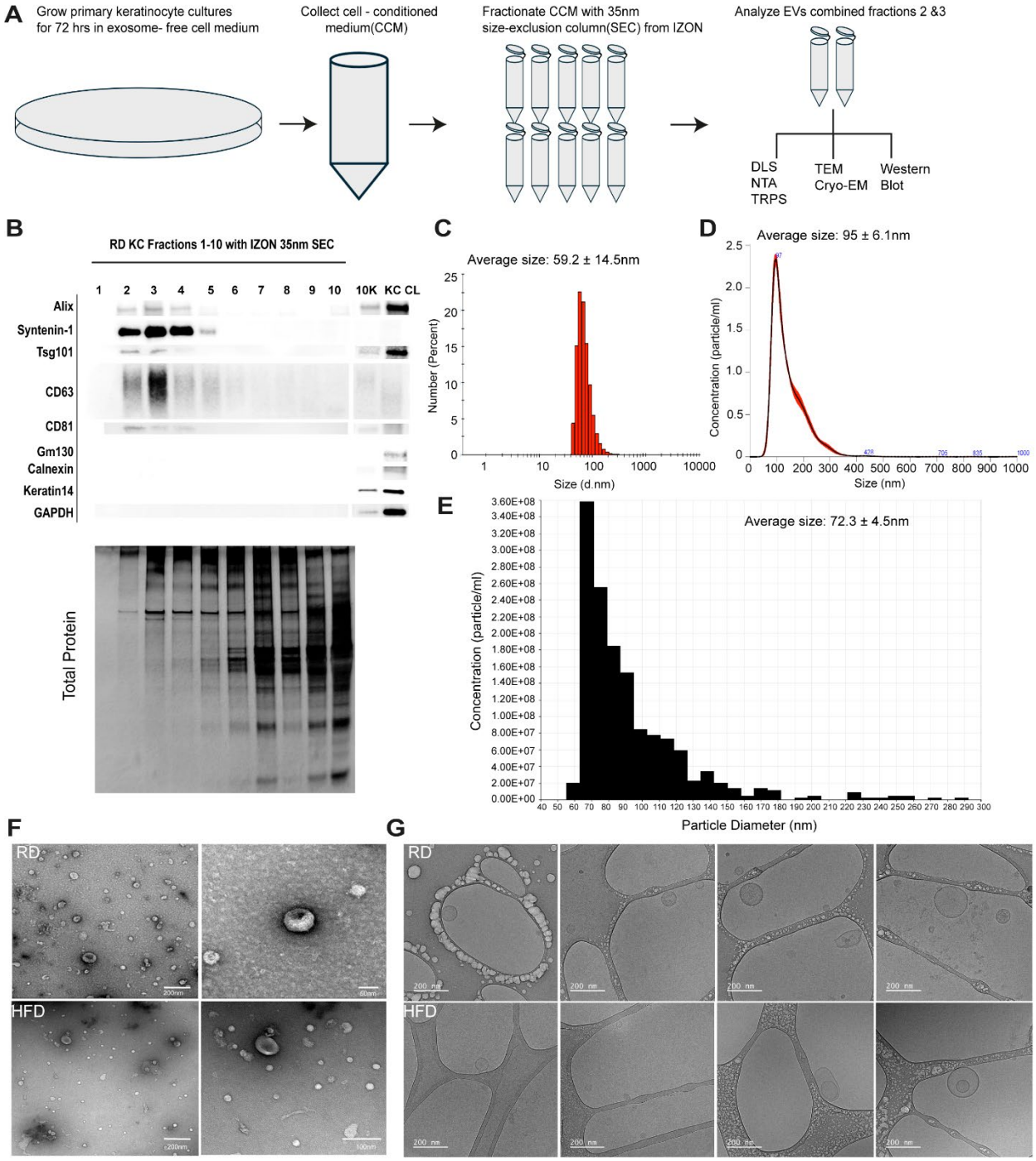

Figure 1: Keratinocytes release a diverse population of exosomes. A) Workflow schematic for keratinocyte-derived exosome (KDE) isolation using size exclusion chromatography (SEC). **B)** Immunoblotting the ten SEC fractions revealed that exosome-associated proteins ALIX, Syntenin, Tsg101, CD63, and CD81 were enriched

356 in fractions 2 and 3 relative to the total protein concentration (silver stain). **C)** KDEs
357 analyzed with dynamic light scattering had a size range of 59.2 ± 14.5nm (mean ±
358 StDev). N=7 across biological replicates from both male and female mice. **D)** KDEs
359 analyzed using nanoparticle tracking analysis produced a concentration peak particle
360 size of 95 ± 6.1 nm (mean ± StDev). N=2 male biological replicates. **E)** KDEs analyzed
361 using tunable resistive pulse sensing (TRPS) determined that the mean size for RD
362 KDEs was 97.7 ± 4.5nm, with a concentration peak of 72.3 ± 4.5nm (mean ± StDev).
363 N=2 biological replicates. **F)** Nanovesicles from combined fraction 2/3 were visualized
364 with negative stain EM. N=11 across 5 biological replicates from male and female mice.
365 **G)** Combined SEC fractions 2/3 were visualized with cryo-EM, demonstrating several
366 diverse populations. N=2 biological replicates, one male and one female.

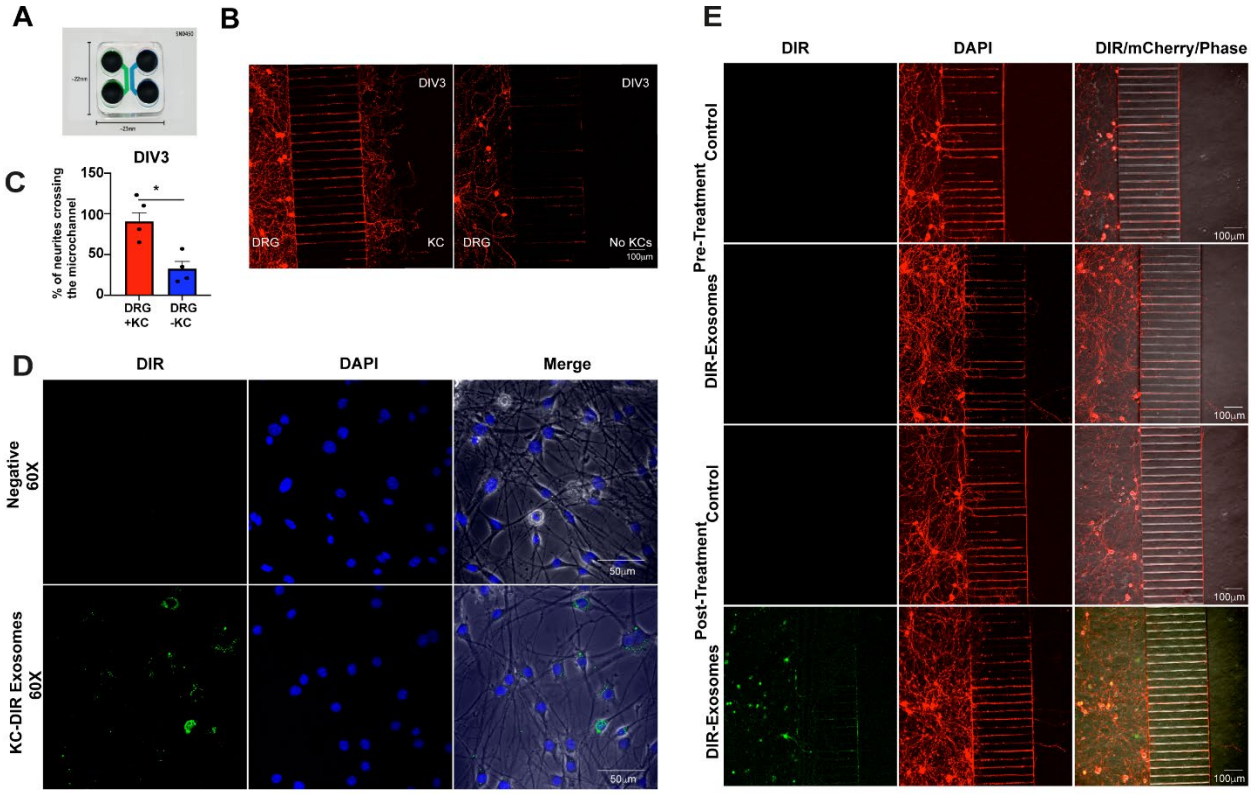

Figure 2: Isolated exosomes from SEC fraction 2/3 are functionally retrogradely trafficked by DRG neurons *in vitro*. A) Representative picture of microfluidics device. **B)** The presence of keratinocytes co-cultured with DRG neurons in a microfluidic paradigm encouraged neurite outgrowth crossing through the microchannels connecting both chambers. **C)** We observed a significant increase in the neurite microchannel crossing when co-cultured in the presence of keratinocytes ($p \leq 0.05$, one-tailed, paired t-test; n=5 with KCs and n=4 without KCs paired with DRG primary cultures). **D)** KDEs from SEC Fr2/3 are functionally internalized by primary DRG neurons. N=4 across 2 biological replicates. **E)** KDEs are retrogradely trafficked into the neuron cell body through the neurites in a microfluidic paradigm. N=4 biological replicates.

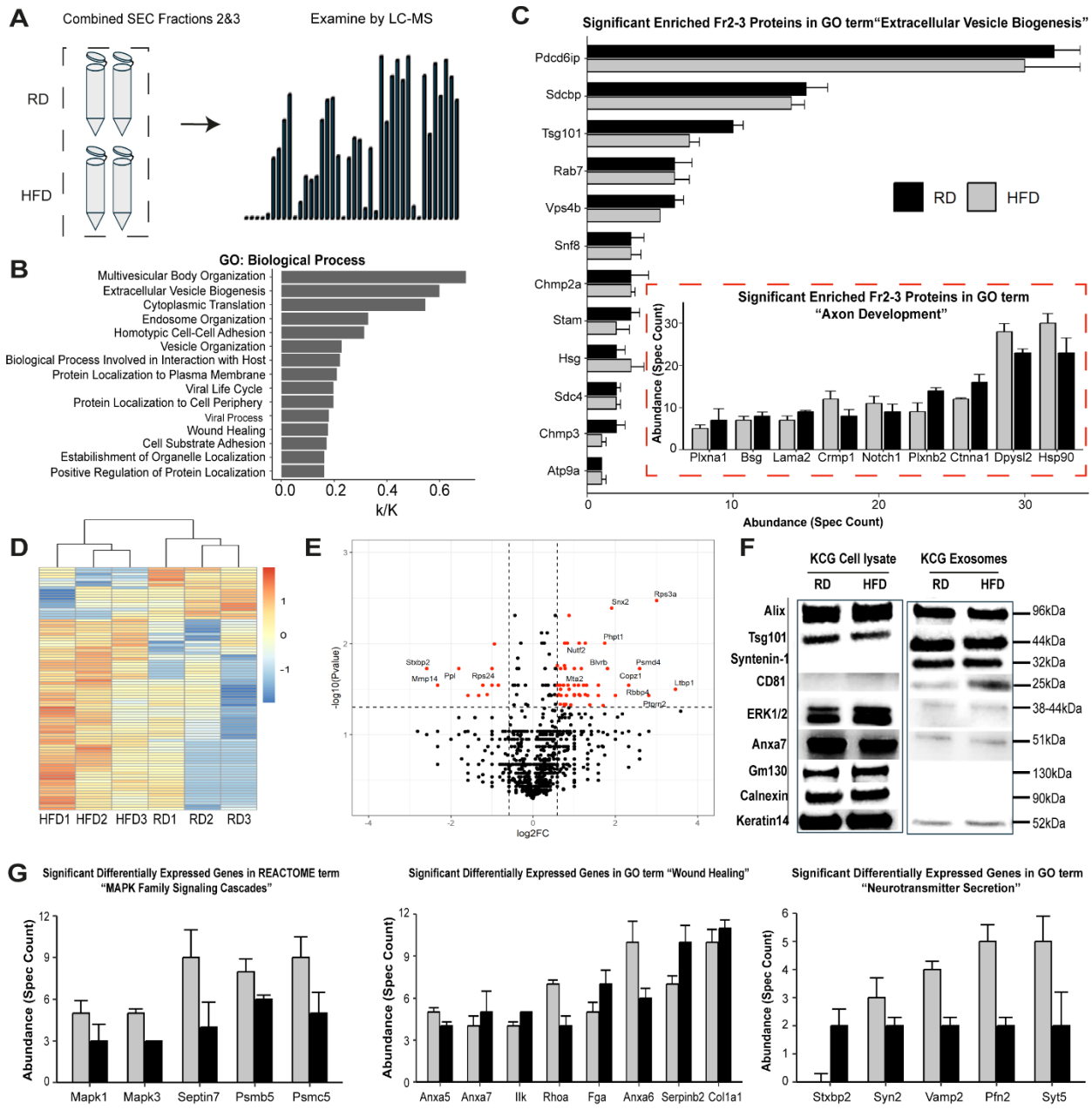

Figure 3: Keratinocyte-derived exosomes (KDEs) significantly alter their protein cargo in painful diabetic neuropathy. A) Workflow schematic depicting exosome proteomic analysis. N=3 biological replicates for each group from male mice. **B)** The top pathways from a gene ontology enrichment analysis of proteins present in each of the three biological replicates in both experimental groups suggested EV enrichment.

382 Bonferroni adjusted p-value ≤ 0.01. **C)** Select panel of proteins associated with GO Term
383 'EV Biogenesis' revealed similar spectral counts for exosome markers Alix, Syntenin-1,
384 and Tsg101 between both groups. Insert: GO Term 'Axon Development' revealed several
385 unverified notable proteins as exosome cargo. Mean ± SEM. GO Terms Bonferroni
386 adjusted p-value ≤ 0.01. **D)** There were 90 significant differentially expressed exosome-
387 associated proteins (EAPs; FC ≥ 1.5 and paired t-test, one-way, p ≤ 0.05) between RD
388 and HFD KDEs that clustered by group. FC calculated as average HFD/RD spectral count
389 for each protein. **E)** Representative volcano plot with 90 EAPs with FC ≥ 1.5 and p ≤ 0.05
390 (labelled red). There were 11 downregulated and 79 upregulated EAPs. **F)** Western blot
391 confirms two EAPs, Mapk1 (via ERK1/2 expression) and annexin-7 in SEC Fr2/3. n=3
392 biological replicates for each group. **G)** Abundances for EAPS in the differentially
393 expressed GO term 'Wound Healing,' 'Neurotransmitter Secretion,' and the REACTOME
394 term 'MAPK Family Signaling Cascades.' Mean ± SEM. Bonferroni adjusted p-value ≤
395 0.01.

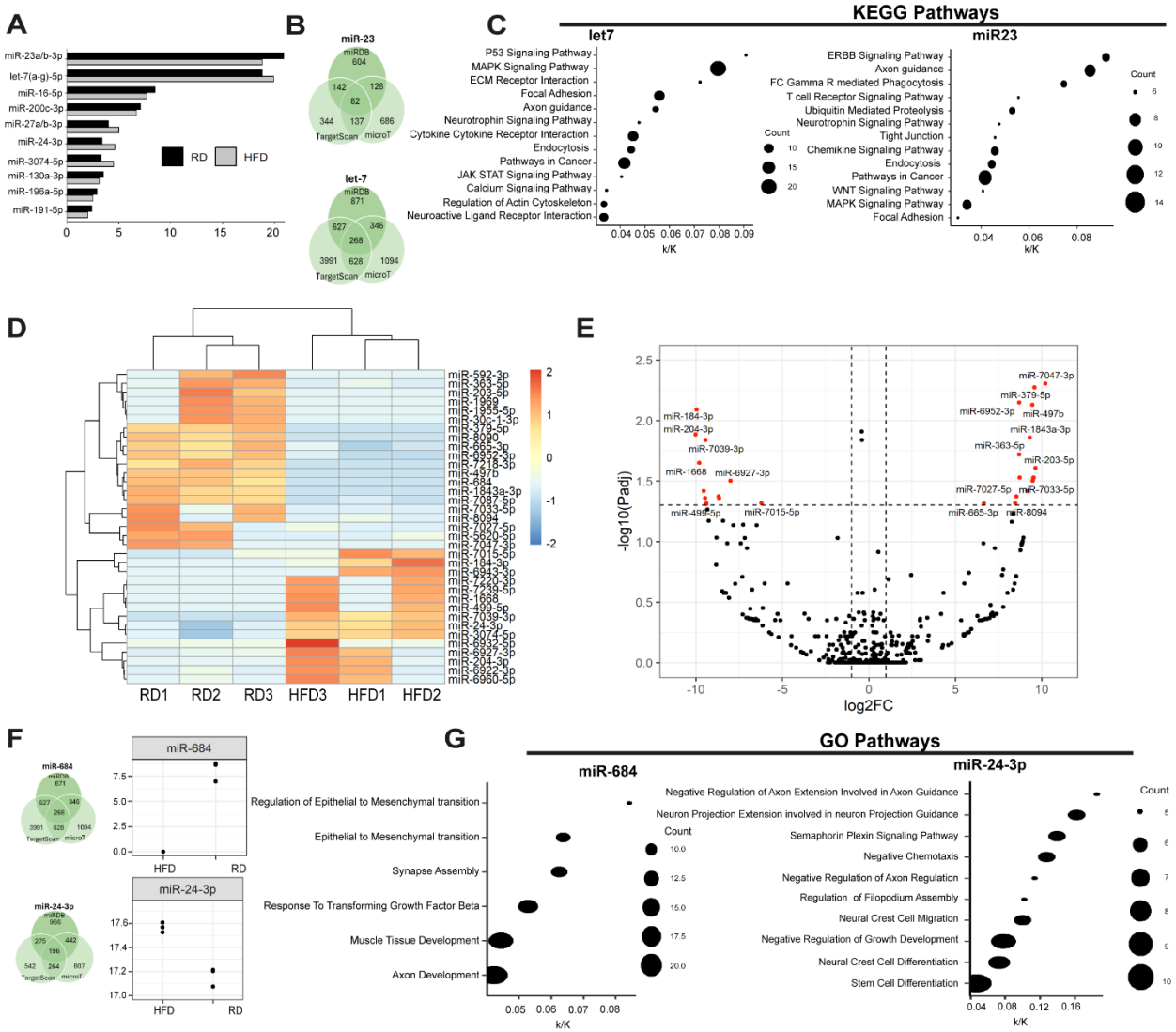

Figure 4: Keratinocyte-derived exosomes (KDEs) alter their small RNA cargo in painful diabetic neuropathy. N=3 biological replicates for male mice in each diet group. A) The top ten small RNAs identified in both RD and HFD KDEs represent 74.8% of the total small RNA sequenced. The top two small RNAs, the let-7 and microRNA-23 families, accounted for almost 40% of the total small RNA sequenced. **B)** The predicted protein targets for let-7 and miR-23 were obtained by cross-referencing 3 separate databases: MirDB, TargetScan, and DIANA-microT. The protein targets predicted by all three programs were used for downstream analysis. **C)** The enrichment analysis of the

404 predicted protein targets of let-7 and miR-23 both revealed predicted KEGG pathways
405 related to 'Axon Guidance,' suggesting a possible role of KDE small RNAs on
406 keratinocyte-to-neuron communication. KEGG pathways Bonferroni adjusted p-value ≤
407 0.01. **D)** There were 35 differentially expressed microRNAs, which clustered by group.
408 Bonferroni adjusted p-value ≤ 0.05. **E)** Of the 33 differentially expressed microRNAs (FC
409 ≥ 1.5, adjusted p-value ≤ 0.05) between RD and HFD, 22 were overexpressed in HFD.
410 FC is defined as HFDavg/RDavg microRNA counts for each small RNA. Bonferroni
411 adjusted p-value. **F)** miR-684 was downregulated in HFD while miR-24-3p was
412 upregulated. Using the same three databases as Figure 4B, predicted target proteins lists
413 were obtained for each. **G)** The gene ontology enrichment analysis for these predicted
414 proteins presented several interesting GO Terms. Both differentially expressed
415 microRNAs predicted axon-related pathways, further providing evidence for an altered
416 keratinocyte-to-neuron communication via exosome cargo. GO Terms Bonferroni
417 adjusted p-value ≤ 0.01.

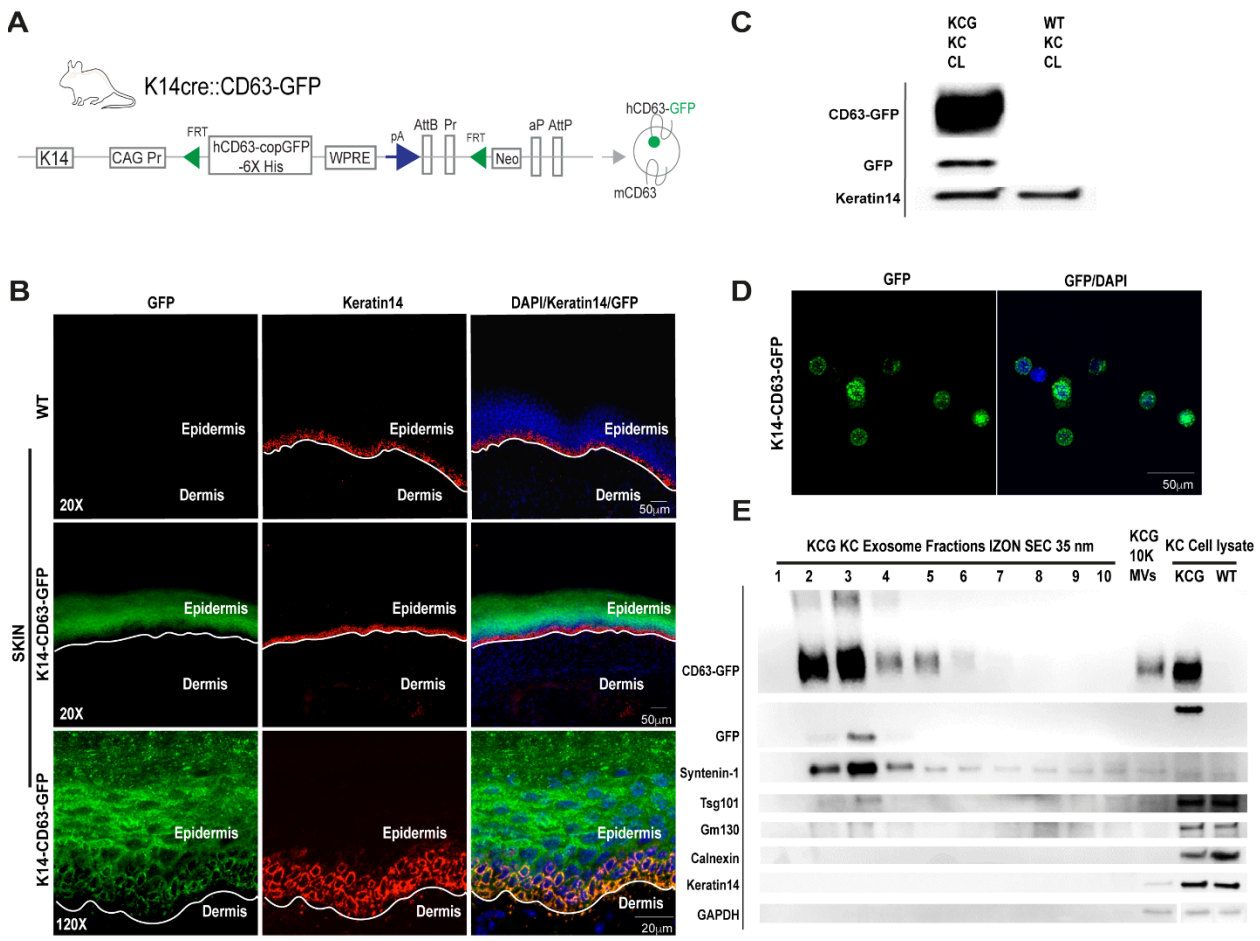

Figure 5: Epidermal keratinocyte-derived exosomes (KDEs) are enriched with GFP in an EV-reporter mouse model. A) We created an EV-reporter mouse line by crossing the commercially available CD63-GFP fl/fl mouse line with K14-Cre to create K14-CD63-GFP (KCG) mice. **B)** IHC on cryo-sections of glabrous mouse skin demonstrated GFP expression in all layers of the epidermis with no detectable GFP in the dermis. The GFP (green) signal also co-localized with K14 staining (red), representing the basal layer of the epidermis. **C)** Immunoblotting revealed robust GFP signal in epidermal cell lysate from our EV-reporter mouse line. **D)** GFP was detected in the primary keratinocyte cultures from our EV-reporter mouse line. **E)** Cell-conditioned medium from KCG keratinocyte cultures was run through IZON 35nm SEC columns. Fraction 2/3 was enriched with

428 CD63-GFP and soluble GFP, supporting that KDEs from primary cultured keratinocytes

429 from our EV-reporter mouse line are tagged with the CD63-GFP fusion protein.

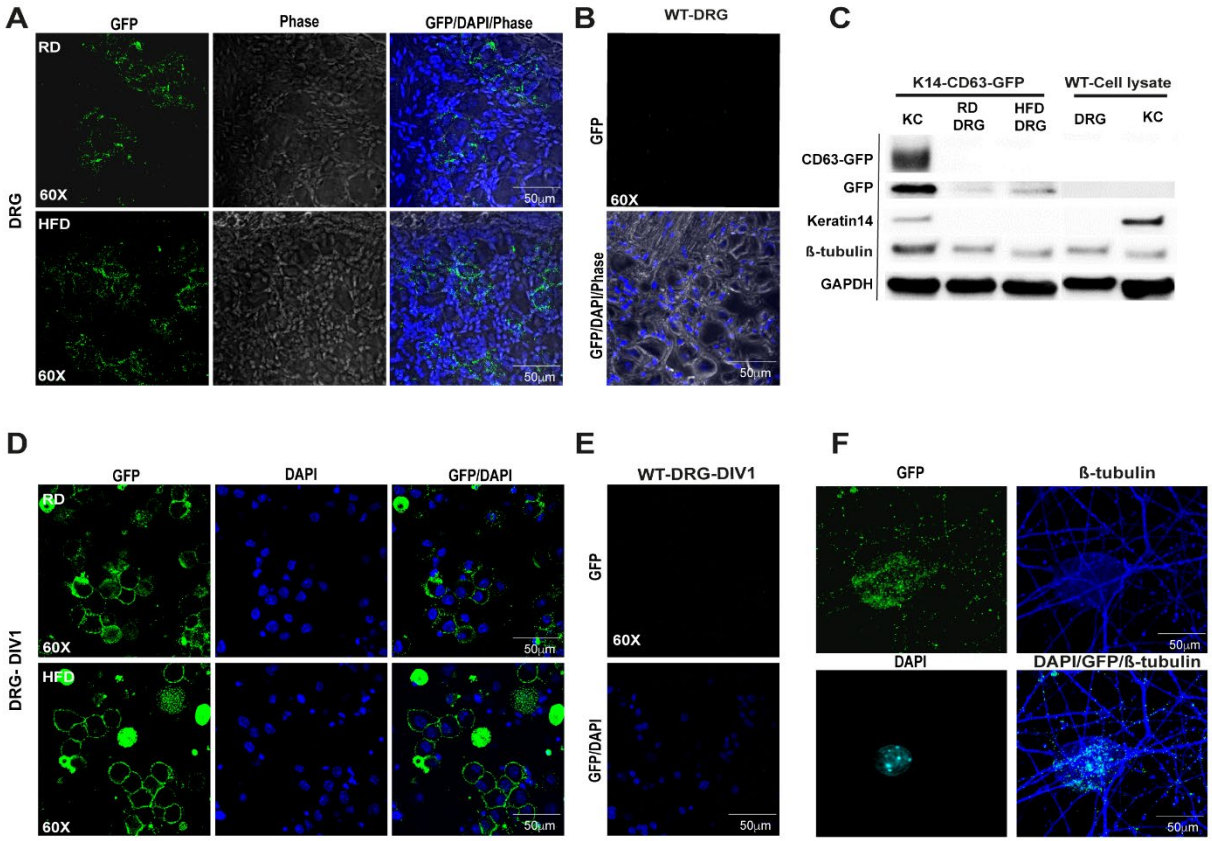

Figure 6: Epidermal keratinocyte-derived exosomes (KDEs) are retrogradely trafficked from the epidermis to DRG neurons *in vivo* in male and female mice. A) We detected GFP signal after immunolabel amplification in cryosections of the DRGs from the EV-reporter mice for both RD and HFD. N=3 male biological replicates for both RD and HFD and n=2 for RD female mice. **B)** As expected, no false GFP signal was detect in WT DRG cryosections. N=3 biological replicates of WT. **C)** Immunoblotting the DRG cell lysate of EV-reporter mice revealed GFP expression. N=2 biological replicates for both RD and HFD. **D)** We detected GFP signal after IHC amplification in primary DRG cell cultures from the EV-reporter mice for both RD and HFD. N=3 biological replicates for both RD and HFD. **E)** As expected, no false GFP signal was detected in WT primary DRG cultures. N=3 biological replicates of WT. **F)** The GFP signal was not only detected

441 in the cell body of the primary DRG cultures from EV-reporter mice but also along the
442 neurites, further providing evidence that KDEs are trafficked along the neurites. N=6
443 biological replicates between RD and HFD.

444 **METHODS**

445 ***Animals*.** Animals were housed on a 12-hour light/12-hour dark cycle with ad libitum
446 access to food and water. We used the following mouse lines: K14-Cre, homozygous;
447 CD63-emGFP fl, homozygous; K14-Cre::CD63-emGFP fl heterogenous.

448 ***HFD*.** Mice were fed 42% fat (Envigo TD88137) for 10 weeks as a rodent model of type 2
449 diabetes. Control mice were fed a regular diet (RD) of 11% fat. After 10 weeks of RD or
450 HFD, a glucose tolerance test was performed as described[49]. A cutoff of (≥140 mg/dl) at
451 2 SD above the mean for glucose 120 minutes after glucose challenge in WT littermate
452 mice was used as a 'diabetic' classification[49].

453 ***Behavioral testing*.** von Frey behavioral studies were performed as previously
454 described[49] with random experimental group assignments and double-blind investigator
455 and endpoint analysis conditions.

456 ***Primary keratinocyte cultures*.** Glabrous paw skin is dissected from the mouse and
457 incubated in dispase (2.3 mg/ml) overnight. The epidermis is separated from the dermis
458 and incubated in TrypLE Express (10 min, 37C; Gibco 12604-013); the keratinocytes are
459 dislodged using gentle agitation with forceps and then plated on 15cm^2 plates with 154CF
460 epidermal medium (M154CF500) supplemented with 170ul of 0.2M $CaCl_2$ and 5ml of
461 HKGS (S-001-5), which was depleted of EVs following 18 hours of ultracentrifugation at
462 100,000*g*. Medium change occurs 24 hours after plating and then every 48 hours.
463 Complete cell culture medium and all other reagents have been confirmed to be EV-free
464 prior to use with the keratinocyte cultures.

465 ***Wound healing scratch assay*.** Primary keratinocyte cultures were grown on 6-well
466 plates (Fisherbrand FB012927) with a 300,000-seeding density and grown to 90%

467 confluency. The tip of an Eppendorf 200ul pipette tip (Fisher 02707409) was used to form
468 a vertical scratch down the center. Cultures were tracked every 24 hours on a Leica 2000
469 LED microscope and analyzed using ImageJ software to measure the rate of gap closure.
470 One-tail paired t-tests were used on the raw dataset to obtain a p-value between groups
471 for each time point (n=58 RD, n=61 HFD for each time point across three separate
472 biological replicates for each group; significance $p \leq 0.05$).

473 ***Exosome isolation with size exclusion columns.*** Cell-conditioned medium from
474 keratinocyte cultures is collected between culture confluency of 60-90%, is centrifuged at
475 3000*g* for 30 minutes to remove cell debris and is then concentrated to 500 µl using
476 centrifuge size filters (Pierce Protein Concentrators PES 10K, 88528). The sample is then
477 run through an IZON SEC qEV 35nm column (IZON, ICO-35) as previously reported[43].
478 Fractions 2-3 are used for downstream applications.

479 ***Western Blot.*** Fractions 1-10 of 400ul each are concentrated to 20ul using Millipore
480 centrifuge filters (Microcon 30kDa, MRCF0R030) and combined with one volume
481 equivalent of BioRad 2x Lammalenni loading buffer (BioRad 1610737) with 5% BME.
482 Each fraction is run through a 3-15% gradient gel (BioRad 45610840) alongside full
483 keratinocyte cell lysate (+) and a 10K pellet (large EVs), running a BCA assay (Thermo
484 Scientific) to load ~3 µg of protein per well. Protein was then transferred to PVDF
485 membranes (Millipore) and blocked (BioRad Everyblot 12010020) for 15 minutes. Primary
486 antibodies are applied overnight at 4 °C with secondary antibody at room temperature for
487 2 hours with 3 TBST washes between each step. Proteins are visualized with a
488 chemiluminescence detection system (Thermo Scientific 32209). All western blot gels
489 were run at minimum in triplicate. Blots were visualized on a Li-Cor Odyssey Fc.

490 ***Western blot antibodies.*** The following primary antibodies were used: Alix (Abcam
491 ab88388), Syntenin-1 (Abcam ab19903), Tsg101 (Invitrogen PA531260), CD63
492 (Invitrogen 2H5I1), CD81 (Abcam ab109201), GM130 (Abcam ab52649), Calnexin
493 (Abcam ab22595), K14 (BioLegend 906004), GFP (Abcam ab13970), β-tubulin
494 (ProteinTech 80713-1-RR100UL), GAPDH (Abcam ab181602). The following secondary
495 antibodies were used: Goat anti-rabbit HRP (Abcam ab97080), Goat anti-chicken HRP
496 (Invitrogen A16054).

497 ***Dynamic light scattering.*** 80ul of samples are pipetted into cuvettes (Malvern
498 Catalog#759200) and run through the zetasizer spectrophotometer (Malvern Zetasizer
499 Nano ZSP) with an EV refractive index of 1.35 in ANTEC through Northwestern University.
500 Malvern analytical software is used to analyze the output using particle counts relative to
501 the signal intensity.

502 ***Negative stain EM.*** Samples suspended in PBS are prepared using the standard uranyl
503 acetate fixation for 5 mins seeded on EMS grids (TMS Catalog#71150) and imaged on a
504 FEI Spirit 2 electron microscope. Images were processed using ImageJ software.

505 ***Cryo-EM.*** CryoEM images are obtained through the northwestern BioCryo core facility
506 (NUANCE) with samples prepared as previously described[92].

507 ***Primary DRG Cultures.*** DRG sensory neurons from WT and K14-CD63-GFP mice were
508 dissociated as described[93] at 18 weeks of age.

509 ***Microfluidics.*** Primary DRG cultures were deposited into one compartment chamber
510 connected to the microchannel column in a microfluidic system (XONA Microfluidics
511 SND450) with or without primary keratinocyte cultures in the other compartment
512 chambers. Keratinocytes were cultured for 3 days before depositing DRG cultures unless

513 otherwise specified. The medium was a combination of 50% DRG culture medium as
514 previously described[93] and 50% keratinocyte culture medium when both cell types were
515 present in the chambers.

516 ***DIR Labelling.*** Concentrated CCM was labeled with DIR (Invitrogen D12731; 2ug/ul) at
517 a ratio of 1:100 by volume and then passed through the IZON 35nm columns. Isolated
518 DIR-labeled exosomes from fractions 2-3 were then used for downstream applications
519 with a negative DIR control, which was DIR-added to concentrated EV-depleted
520 unconditioned medium passed through the column with the same fractions collected for
521 experiments.

522 ***DIR-Exosomes***. DRG Cultures: DIR-labeled exosomes were directly applied to DIV-1
523 primary DRG cultures and visualized after 16 hours post-treatment by confocal
524 microscopy. Microfluidics: DIR-exosomes were applied to the empty compartment after
525 DRG neuron neurites occupied all microchannels, preventing medium exchange between
526 the two compartments. The microfluidic chambers were visualized after 16 hours by
527 confocal microscopy.

528 ***MS sample preparation***

529 Trichloroacetic acid (TCA, Sigma-Aldrich, Cat# T0699) precipitation was used to clean
530 and precipitate proteins from EV samples. Protein pellets were resuspended in 8 M urea
531 (ThermoFisher Scientific, Cat # 29700) prepared in 100 mM ammonium bicarbonate
532 solution (Fluka, Cat # 09830) and processed with ProteaseMAX (Promega, Cat # V2072)
533 according to the manufacturer's protocol. The samples were reduced with 5 mM Tris(2-
534 carboxyethyl)phosphine (TCEP, Sigma-Aldrich, Cat # C4706; vortexed for 1 hour at RT),
535 alkylated in the dark with 10 mM iodoacetamide (IAA, Sigma-Aldrich, Cat # I1149; 20 min

536 at RT), diluted with 100 mM ABC, and quenched with 25 mM TCEP. Samples were diluted
537 with 100 mM ammonium bicarbonate solution, and digested with Trypsin (1:50, Promega,
538 Cat # V5280) for overnight incubation at 37°C with intensive agitation. The next day,
539 reaction was quenched by adding 1% trifluoroacetic acid (TFA, Fisher Scientific, O4902-
540 100). The samples were desalted using Peptide Desalting Spin Columns (Thermo Fisher
541 Scientific, Cat # 89882). All samples were vacuum centrifuged to dry.

542 ***Tandem Mass spectrometry***

543 Three micrograms of each sample were auto-sampler loaded with a Thermo Vanquish
544 Neo UHPLC system onto a PepMap™ Neo Trap Cartridge (Thermo Fisher Scientific,
545 Cat#: 174500, diameter, 300 µm, length, 5 mm, particle size, 5 □m, pore size, 100 Å,
546 stationary phase, C18) coupled to a nanoViper analytical column (Thermo Fisher
547 Scientific, Cat#: 164570, diameter, 0.075 mm, length, 500 mm, particle size, 3 µm, pore
548 size, 100 Å, stationary phase, C18) with stainless steel emitter tip assembled on the
549 Nanospray Flex Ion Source with a spray voltage of 2000 V. An Orbitrap Ascend (Thermo
550 Fisher Scientific) was used to acquire all the MS spectral data. Buffer A contained 99.9%
551 H2O and 0.1% FA, and buffer B contained 80.0% ACN, 19.9% H2O with 0.1% FA. For
552 each fraction, the chromatographic run was for 2 hours in total with the following profile:
553 0-8% for 6, 8% for 64, 24% for 20, 36% for 10, 55% for 10, 95% for 10 and again 95% for
554 6 We used Orbitrap HCD-MS2 method for these experiments. Briefly, ion transfer tube
555 temp = 275 °C, Easy-IC internal mass calibration, default charge state = 2 and cycle time
556 = 3 s. Detector type set to Orbitrap, with 60K resolution, with wide quad isolation, mass
557 range = normal, scan range = 375-1500 m/z, max injection time mode = Auto, AGC target
558 = Standard, microscans = 1, S-lens RF level = 60, without source fragmentation, and

559 datatype = Profile. MIPS was set as on, included charge states = 2-7 (reject unassigned).
560 Dynamic exclusion enabled with n = 1 for 60s exclusion duration at 10 ppm for high and
561 low with Exclude Isotopes. Isolation Mode = Quadrupole, isolation window = 1.6, isolation
562 Offset = Off, active type = HCD, collision energy mode = Fixed, HCD collision energy type
563 = Normalized, HCD collision energy = 25%, detector type = Orbitrap, orbitrap resolution
564 = 15K, mass range = Normal, scan range mode = Auto, max injection time mode = Auto,
565 AGC target = Standard, Microscans = 1, data type = Centroid.mins receptively.

566 ***MS data analysis and quantification***

567 Protein identification/quantification and analysis were performed with Integrated
568 Proteomics Pipeline - IP2 (Bruker, Madison, WI. http://www.integratedproteomics.com/)
569 using ProLuCID[94,95], DTASelect2[96,97], Census and Quantitative Analysis. Spectrum raw
570 files were extracted into MS1, MS2 files using RawConverter
571 (http://fields.scripps.edu/downloads.php). The tandem mass spectra (raw files from the
572 same sample were searched together) were searched against UniProt mouse
573 (downloaded on 07-29-2023) protein databases[98] and matched to sequences using the
574 ProLuCID/SEQUEST algorithm (ProLuCID version 3.1) with 50 ppm peptide mass
575 tolerance for precursor ions and 600 ppm for fragment ions. The search space included
576 all fully and half-tryptic peptide candidates within the mass tolerance window with no-
577 miscleavage constraint, assembled, and filtered with DTASelect2 through IP2. To
578 estimate protein probabilities and false-discovery rates (FDR) accurately, we used a
579 target/decoy database containing the reversed sequences of all the proteins appended
580 to the target database[98] (UniProt, 2015). Each protein identified was required to have a
581 minimum of one peptide of minimal length of six amino acid residues. After the

582 peptide/spectrum matches were filtered, we estimated that the protein FDRs were ≤ 1%
583 for each sample analysis. Resulting protein lists include subset proteins to allow for
584 consideration of all possible protein isoforms implicated by at least three given peptides
585 identified from the complex protein mixtures. Then, we used Census and Quantitative
586 Analysis in IP2 for protein quantification. Static modification: 57.02146 C for
587 carbamidomethylation. Quantification was performed by the built-in module in IP2.

588 ***Proteomics Statistics.*** The spectral counts for each protein accession ID for the three
589 RD and HFD biological replicates are used to run a one-tailed, paired t-test for statistical
590 significance. The average spectral counts for RD and HFD were used to obtain a HFD/RD
591 fold change. The volcano plot was generated in R using ggplot2. The heat map was
592 generated using the R package pheatmap. Gene ontology enrichment analyses were
593 generated using the R packages clusterprofiler, msigdbr and ggplot2. GO enrichment
594 analyses used proteins present in all biological replicates of each group only.

595 ***Small RNA sequencing.*** Samples underwent small RNA sequencing through
596 Northwestern's core facilities. Biological triplicate RD and HFD RNA samples were
597 prepared using the total exosome RNA and protein extraction kit from Invitrogen
598 (Invitrogen Catalog#2743605). RNA samples were quantified by Qubit RNA HS assay
599 and the quality was confirmed by Bioanalyzer RNA pico chip assay. Then, 1ng of RNA
600 was used as input for library preparation with NextFlex small RNA-seq kit v4 according to
601 manufacturer's protocol. Each sample was barcoded with a unique index and multiplexed
602 libraries were pooled for sequencing on Novaseq X Plus 10B flowcell using single end
603 50nt mode.

604 ***RNA sequencing Statistics.*** Data analysis was carried out in R using the standard
605 workflow of DESeq2 paired with the libraries apeglm and ggplot2 for figure generation.
606 Bonferroni post-hoc adjustment was used for the reported adjusted p-values ≤ 0.05 for
607 significance. Gene ontology enrichment analyses were generated using the R packages
608 clusterprofiler, msigdbr and ggplot2 with Bonferroni post-hoc adjusted P values < 0.05 for
609 significance.

610 ***Protein target analysis.*** The direct or indirect protein targets for each microRNA was
611 predicted using several target prediction programs, including miRDB (http://mirdb.org/)[99],
612 TargetScan v7.0 (http://www.targetscan.org/vert_72/) and DIANA-microT v5.0
613 (https://bio.tools/DIANA-microT). Only the predicted proteins identified by all 3 programs
614 were included in the subsequent enrichment analyses.

615 ***Immunohistochemistry.*** Glabrous hind paw dermis/epidermis was separated from the
616 paw and whole DRGs (lumber 2-4) were isolated from 18 week old mice and fixed with
617 4% PFA for 1 hour, 30% sucrose for 1 hour, and then embedded in OCT. Samples were
618 processed as previously described[50] and analyzed by confocal microscopy.

619 ***Antibodies.*** We used the following primary antibodies on DRG sections: GFP (chicken;
620 Abcam ab13970). We used the following antibodies on skin sections: K14 (BioLegend
621 906004). We used the following antibodies on primary DRG cultures: GFP (Abcam
622 ab13970), β-tubulin (ProteinTech 80713-1-RR100UL). We used the following secondary
623 antibodies: Goat anti-chicken AlexaFluor™-598 (Invitrogen A-11042), goat anti-rabbit
624 AlexaFluor-647 (Invitrogen A32733).

625 ***EV-Reporter Mouse.*** The commercially available CD63-GFP fl/fl mouse line (Jackson
626 Laboratory Strain#:036865) was crossed with K14-Cre mice to generate the EV-reporter
627 K14-CD63-GFP mouse line.
628 ***Study approval.*** All methods involving animals were approved by the IACUC of
629 Northwestern University.
630

631 **ACKNOWLEDGEMENTS**

632 Zetasizer Nano ZSP (DLS), Nanosight (NTA), and IZON Exoid (TRPS) experiments were
633 performed in the Analytical bioNanoTechnology Equipment Core Facility of the Simpson
634 Querrey Institute for BioNanotechnology at Northwestern University. ANTEC receives
635 partial support from the Soft and Hybrid Nanotechnology Experimental (SHyNE)
636 Resource (NSF ECCS-2025633) and Feinberg School of Medicine, Northwestern
637 University. Electron microscopy imaging work was performed at the Northwestern
638 University Center for Advanced Microscopy (RRID: SCR_020996) generously supported
639 by NCI CCSG P30 CA060553 awarded to the Robert H Lurie Comprehensive Cancer
640 Center. This work made use of the EPIC facility of Northwestern University's
641 NUANCE Center, which has received support from the SHyNE Resource (NSF ECCS-
642 2025633), the IIN, and Northwestern's MRSEC program (NSF DMR-2308691). And this
643 work was supported by the Northwestern University NUSeq Core Facility.
644

645 **STATEMENT OF DATA AND MATERIALS**

646 We will make the raw MS data publicly available in an accessible database upon
647 acceptance.

648 ## REFERENCES

649 1 Martin, S. S. *et al.* 2024 Heart Disease and Stroke Statistics: A Report of US and Global Data From
650 the American Heart Association. *Circulation* **149**, e347-e913 (2024).
651 https://doi.org/10.1161/CIR.0000000000001209
652 2 American Diabetes, A. Diagnosis and classification of diabetes mellitus. *Diabetes care* **34 Suppl 1**,
653 S62-69 (2011). https://doi.org/10.2337/dc11-S062
654 3 Dyck, P. J. *et al.* The Rochester Diabetic Neuropathy Study: design, criteria for types of neuropathy,
655 selection bias, and reproducibility of neuropathic tests. *Neurology* **41**, 799-807 (1991).
656 4 Spallone, V., Lacerenza, M., Rossi, A., Sicuteri, R. & Marchettini, P. Painful diabetic polyneuropathy:
657 approach to diagnosis and management. *The Clinical journal of pain* **28**, 726-743 (2012).
658 https://doi.org/10.1097/AJP.0b013e318243075c
659 5 Abbott, C. A., Malik, R. A., van Ross, E. R., Kulkarni, J. & Boulton, A. J. Prevalence and characteristics
660 of painful diabetic neuropathy in a large community-based diabetic population in the U.K. *Diabetes*
661 *care* **34**, 2220-2224 (2011). https://doi.org/10.2337/dc11-1108
662 6 daCosta DiBonaventura, M., Cappelleri, J. C. & Joshi, A. V. A longitudinal assessment of painful
663 diabetic peripheral neuropathy on health status, productivity, and health care utilization and cost.
664 *Pain medicine* **12**, 118-126 (2011). https://doi.org/10.1111/j.1526-4637.2010.01012.x
665 7 Bril, V. *et al.* Evidence-based guideline: Treatment of painful diabetic neuropathy: report of the
666 American Academy of Neurology, the American Association of Neuromuscular and
667 Electrodiagnostic Medicine, and the American Academy of Physical Medicine and Rehabilitation.
668 *Neurology* **76**, 1758-1765 (2011). https://doi.org/10.1212/WNL.0b013e3182166ebe
669 8 Quilici, S. *et al.* Meta-analysis of duloxetine vs. pregabalin and gabapentin in the treatment of
670 diabetic peripheral neuropathic pain. *BMC neurology* **9**, 6 (2009). https://doi.org/10.1186/1471-
671 2377-9-6
672 9 Callaghan, B. C., Cheng, H. T., Stables, C. L., Smith, A. L. & Feldman, E. L. Diabetic neuropathy:
673 clinical manifestations and current treatments. *Lancet Neurol* **11**, 521-534 (2012).
674 https://doi.org/10.1016/S1474-4422(12)70065-0
675 10 Finnerup, N. B. *et al.* Pharmacotherapy for neuropathic pain in adults: a systematic review and
676 meta-analysis. *Lancet Neurol* **14**, 162-173 (2015). https://doi.org/10.1016/S1474-4422(14)70251-
677 0
678 11 Attal, N. & Bouhassira, D. Advances in the treatment of neuropathic pain. *Curr Opin Neurol* **34**,
679 631-637 (2021). https://doi.org/10.1097/WCO.0000000000000980
680 12 Shinu, P. *et al.* Novel Therapies for the Treatment of Neuropathic Pain: Potential and Pitfalls. *J Clin*
681 *Med* **11** (2022). https://doi.org/10.3390/jcm11113002
682 13 Lauria, G. & Devigili, G. Skin biopsy as a diagnostic tool in peripheral neuropathy. *Nat Clin Pract*
683 *Neurol* **3**, 546-557 (2007). https://doi.org/10.1038/ncpneuro0630
684 14 Sommer, C. & Lauria, G. Skin biopsy in the management of peripheral neuropathy. *The Lancet.*
685 *Neurology* **6**, 632-642 (2007). https://doi.org/10.1016/S1474-4422(07)70172-2
686 15 Stucky, C. L. & Mikesell, A. R. Cutaneous pain in disorders affecting peripheral nerves. *Neuroscience*
687 *letters* **765**, 136233 (2021). https://doi.org/10.1016/j.neulet.2021.136233
688 16 Mikesell, A. R. *et al.* Keratinocyte PIEZO1 modulates cutaneous mechanosensation. *Elife* **11** (2022).
689 https://doi.org/10.7554/eLife.65987
690 17 Moehring, F. *et al.* Keratinocytes mediate innocuous and noxious touch via ATP-P2X4 signaling.
691 *Elife* **7** (2018). https://doi.org/10.7554/eLife.31684
692 18 Sadler, K. E., Moehring, F. & Stucky, C. L. Keratinocytes contribute to normal cold and heat
693 sensation. *Elife* **9** (2020). https://doi.org/10.7554/eLife.58625

19 Radtke, C., Vogt, P. M., Devor, M. & Kocsis, J. D. Keratinocytes acting on injured afferents induce extreme neuronal hyperexcitability and chronic pain. *Pain* **148**, 94-102 (2010). https://doi.org/10.1016/j.pain.2009.10.014

20 Talagas, M. *et al.* Keratinocytes Communicate with Sensory Neurons via Synaptic-like Contacts. *Annals of neurology* **88**, 1205-1219 (2020). https://doi.org/10.1002/ana.25912

21 Erbacher, C. *et al.* Interaction of human keratinocytes and nerve fiber terminals at the neuro-cutaneous unit. *Elife* **13** (2024). https://doi.org/10.7554/eLife.77761

22 van Niel, G., D'Angelo, G. & Raposo, G. Shedding light on the cell biology of extracellular vesicles. *Nat Rev Mol Cell Biol* **19**, 213-228 (2018). https://doi.org/10.1038/nrm.2017.125

23 Mathieu, M., Martin-Jaular, L., Lavieu, G. & Thery, C. Specificities of secretion and uptake of exosomes and other extracellular vesicles for cell-to-cell communication. *Nat Cell Biol* **21**, 9-17 (2019). https://doi.org/10.1038/s41556-018-0250-9

24 Gurung, S., Perocheau, D., Touramanidou, L. & Baruteau, J. The exosome journey: from biogenesis to uptake and intracellular signalling. *Cell Commun Signal* **19**, 47 (2021). https://doi.org/10.1186/s12964-021-00730-1

25 Kalluri, R. & LeBleu, V. S. The biology, function, and biomedical applications of exosomes. *Science* **367** (2020). https://doi.org/10.1126/science.aau6977

26 Pan, B. T., Teng, K., Wu, C., Adam, M. & Johnstone, R. M. Electron microscopic evidence for externalization of the transferrin receptor in vesicular form in sheep reticulocytes. *The Journal of cell biology* **101**, 942-948 (1985). https://doi.org/10.1083/jcb.101.3.942

27 Rastogi, S. *et al.* The Evolving Landscape of Exosomes in Neurodegenerative Diseases: Exosomes Characteristics and a Promising Role in Early Diagnosis. *Int J Mol Sci* **22** (2021). https://doi.org/10.3390/ijms22010440

28 Fan, Y., Chen, Z. & Zhang, M. Role of exosomes in the pathogenesis, diagnosis, and treatment of central nervous system diseases. *J Transl Med* **20**, 291 (2022). https://doi.org/10.1186/s12967-022-03493-6

29 Dai, J. *et al.* Exosomes: key players in cancer and potential therapeutic strategy. *Signal Transduct Target Ther* **5**, 145 (2020). https://doi.org/10.1038/s41392-020-00261-0

30 Lo Cicero, A. *et al.* Exosomes released by keratinocytes modulate melanocyte pigmentation. *Nature communications* **6**, 7506 (2015). https://doi.org/10.1038/ncomms8506

31 Nasiri, G., Azarpira, N., Alizadeh, A., Goshtasbi, S. & Tayebi, L. Shedding light on the role of keratinocyte-derived extracellular vesicles on skin-homing cells. *Stem Cell Res Ther* **11**, 421 (2020). https://doi.org/10.1186/s13287-020-01929-8

32 Zhou, X. *et al.* Exosome-Mediated Crosstalk between Keratinocytes and Macrophages in Cutaneous Wound Healing. *ACS Nano* **14**, 12732-12748 (2020). https://doi.org/10.1021/acsnano.0c03064

33 Jiang, M. *et al.* Keratinocyte exosomes activate neutrophils and enhance skin inflammation in psoriasis. *FASEB journal : official publication of the Federation of American Societies for Experimental Biology* **33**, 13241-13253 (2019). https://doi.org/10.1096/fj.201900642R

34 Kotzerke, K. *et al.* Immunostimulatory activity of murine keratinocyte-derived exosomes. *Exp Dermatol* **22**, 650-655 (2013). https://doi.org/10.1111/exd.12230

35 Ai, M. *et al.* Role of Human Mesenchymal Stem Cells and Derived Extracellular Vesicles in Reducing Sensory Neuron Hyperexcitability and Pain Behaviors in Murine Osteoarthritis. *Arthritis Rheumatol* **75**, 352-363 (2023). https://doi.org/10.1002/art.42353

36 Ashrafizadeh, M., Kumar, A. P., Aref, A. R., Zarrabi, A. & Mostafavi, E. Exosomes as Promising Nanostructures in Diabetes Mellitus: From Insulin Sensitivity to Ameliorating Diabetic Complications. *Int J Nanomedicine* **17**, 1229-1253 (2022). https://doi.org/10.2147/IJN.S350250

741 37 Sun, Y. *et al.* Human Mesenchymal Stem Cell Derived Exosomes Alleviate Type 2 Diabetes Mellitus
742 by Reversing Peripheral Insulin Resistance and Relieving beta-Cell Destruction. *ACS Nano* **12**, 7613-
743 7628 (2018). https://doi.org/10.1021/acsnano.7b07643
744 38 He, Q. *et al.* Mesenchymal stem cell-derived exosomes exert ameliorative effects in type 2 diabetes
745 by improving hepatic glucose and lipid metabolism via enhancing autophagy. *Stem Cell Res Ther*
746 **11**, 223 (2020). https://doi.org/10.1186/s13287-020-01731-6
747 39 Wei, P. *et al.* Exosomes derived from human amniotic epithelial cells accelerate diabetic wound
748 healing via PI3K-AKT-mTOR-mediated promotion in angiogenesis and fibroblast function. *Burns*
749 *Trauma* **8**, tkaa020 (2020). https://doi.org/10.1093/burnst/tkaa020
750 40 Fan, B. *et al.* Mesenchymal stromal cell-derived exosomes ameliorate peripheral neuropathy in a
751 mouse model of diabetes. *Diabetologia* **63**, 431-443 (2020). https://doi.org/10.1007/s00125-019-
752 05043-0
753 41 Ahmed, L. A. & Al-Massri, K. F. Exploring the Role of Mesenchymal Stem Cell-Derived Exosomes in
754 Diabetic and Chemotherapy-Induced Peripheral Neuropathy. *Mol Neurobiol* (2024).
755 https://doi.org/10.1007/s12035-024-03916-z
756 42 Jia, L. *et al.* Exosomes derived from high-glucose-stimulated Schwann cells promote development
757 of diabetic peripheral neuropathy. *FASEB journal : official publication of the Federation of*
758 *American Societies for Experimental Biology* **32**, fj201800597R (2018).
759 https://doi.org/10.1096/fj.201800597R
760 43 Böing, A. N. *et al.* Single-step isolation of extracellular vesicles by size-exclusion chromatography.
761 *J Extracell Vesicles* **3** (2014). https://doi.org/10.3402/jev.v3.23430
762 44 Arya, S. B., Collie, S. P. & Parent, C. A. The ins-and-outs of exosome biogenesis, secretion, and
763 internalization. *Trends Cell Biol* **34**, 90-108 (2024). https://doi.org/10.1016/j.tcb.2023.06.006
764 45 Théry, C. *et al.* Minimal information for studies of extracellular vesicles 2018 (MISEV2018): a
765 position statement of the International Society for Extracellular Vesicles and update of the
766 MISEV2014 guidelines. *J Extracell Vesicles* **7**, 1535750 (2018).
767 https://doi.org/10.1080/20013078.2018.1535750
768 46 Wang, Y. Z. *et al.* Notch receptor-ligand binding facilitates extracellular vesicle-mediated neuron-
769 to-neuron communication. *Cell Rep* **43**, 113680 (2024).
770 https://doi.org/10.1016/j.celrep.2024.113680
771 47 George, D. S. *et al.* Mitochondrial calcium uniporter deletion prevents painful diabetic neuropathy
772 by restoring mitochondrial morphology and dynamics. *Pain* (2021).
773 https://doi.org/10.1097/j.pain.0000000000002391
774 48 George, D. S. *et al.* The Mas-related G protein-coupled receptor d (Mrgprd) mediates pain
775 hypersensitivity in painful diabetic neuropathy. *Pain* (2024).
776 https://doi.org/10.1097/j.pain.0000000000003120
777 49 Jayaraj, N. D. *et al.* Reducing CXCR4-mediated nociceptor hyperexcitability reverses painful
778 diabetic neuropathy. *The Journal of clinical investigation* **128**, 2205-2225 (2018).
779 https://doi.org/10.1172/JCI92117
780 50 Menichella, D. M. *et al.* CXCR4 chemokine receptor signaling mediates pain in diabetic neuropathy.
781 *Molecular pain* **10**, 42 (2014). https://doi.org/10.1186/1744-8069-10-42
782 51 Dam, D. H. M. *et al.* Ganglioside GM3 Mediates Glucose-Induced Suppression of IGF-1 Receptor-
783 Rac1 Activation to Inhibit Keratinocyte Motility. *J Invest Dermatol* **137**, 440-448 (2017).
784 https://doi.org/10.1016/j.jid.2016.09.028
785 52 Nowak, N. C., Menichella, D. M., Miller, R. & Paller, A. S. Cutaneous innervation in impaired diabetic
786 wound healing. *Transl Res* **236**, 87-108 (2021). https://doi.org/10.1016/j.trsl.2021.05.003
787 53 Frühbeis, C. *et al.* Oligodendrocytes support axonal transport and maintenance via exosome
788 secretion. *PLoS Biol* **18**, e3000621 (2020). https://doi.org/10.1371/journal.pbio.3000621

54 Graykowski, D. R., Wang, Y. Z., Upadhyay, A. & Savas, J. N. The Dichotomous Role of Extracellular Vesicles in the Central Nervous System. *iScience* **23**, 101456 (2020). https://doi.org/10.1016/j.isci.2020.101456

55 Greenhalgh, D. G. Wound healing and diabetes mellitus. *Clin Plast Surg* **30**, 37-45 (2003). https://doi.org/10.1016/s0094-1298(02)00066-4

56 Häger, S. C. & Nylandsted, J. Annexins: players of single cell wound healing and regeneration. *Commun Integr Biol* **12**, 162-165 (2019). https://doi.org/10.1080/19420889.2019.1676139

57 Creutz, C. E. The annexins and exocytosis. *Science* **258**, 924-931 (1992). https://doi.org/10.1126/science.1439804

58 Sønder, S. L. *et al.* Annexin A7 is required for ESCRT III-mediated plasma membrane repair. *Sci Rep* **9**, 6726 (2019). https://doi.org/10.1038/s41598-019-43143-4

59 Williams, J. K., Ngo, J. M., Lehman, I. M. & Schekman, R. Annexin A6 mediates calcium-dependent exosome secretion during plasma membrane repair. *Elife* **12** (2023). https://doi.org/10.7554/eLife.86556

60 Fan, B., Chopp, M., Zhang, Z. G. & Liu, X. S. Emerging Roles of microRNAs as Biomarkers and Therapeutic Targets for Diabetic Neuropathy. *Front Neurol* **11**, 558758 (2020). https://doi.org/10.3389/fneur.2020.558758

61 Ibrahim, H. M., AlZahrani, A., Hanieh, H., Ahmed, E. A. & Thirugnanasambantham, K. MicroRNA-7188-5p and miR-7235 regulates Multiple sclerosis in an experimental mouse model. *Mol Immunol* **139**, 157-167 (2021). https://doi.org/10.1016/j.molimm.2021.07.002

62 Mukherjee, S., Shelar, B. & Krishna, S. Versatile role of miR-24/24-1*/24-2* expression in cancer and other human diseases. *Am J Transl Res* **14**, 20-54 (2022).

63 Cui, M. *et al.* Interactive functions of microRNAs in the miR-23a-27a-24-2 cluster and the potential for targeted therapy in cancer. *J Cell Physiol* **235**, 6-16 (2020). https://doi.org/10.1002/jcp.28958

64 Lin, Z. *et al.* miR-24-3p Dominates the Proliferation and Differentiation of Chicken Intramuscular Preadipocytes by Blocking ANXA6 Expression. *Genes (Basel)* **13** (2022). https://doi.org/10.3390/genes13040635

65 Herrera, A. *et al.* Neurogenesis redirects β-catenin from adherens junctions to the nucleus to promote axonal growth. *Development* **150** (2023). https://doi.org/10.1242/dev.201651

66 Huang, Y. L. *et al.* Inhibition of Wnt/β-catenin signaling attenuates axonal degeneration in models of Parkinson's disease. *Neurochem Int* **159**, 105389 (2022). https://doi.org/10.1016/j.neuint.2022.105389

67 Duraikannu, A., Martinez, J. A., Chandrasekhar, A. & Zochodne, D. W. Expression and Manipulation of the APC-β-Catenin Pathway During Peripheral Neuron Regeneration. *Sci Rep* **8**, 13197 (2018). https://doi.org/10.1038/s41598-018-31167-1

68 Lewallen, K. A. *et al.* Assessing the role of the cadherin/catenin complex at the Schwann cell-axon interface and in the initiation of myelination. *The Journal of neuroscience : the official journal of the Society for Neuroscience* **31**, 3032-3043 (2011). https://doi.org/10.1523/jneurosci.4345-10.2011

69 Alto, L. T. & Terman, J. R. Semaphorins and their Signaling Mechanisms. *Methods in molecular biology* **1493**, 1-25 (2017). https://doi.org/10.1007/978-1-4939-6448-2_1

70 Janssen, B. J. *et al.* Structural basis of semaphorin-plexin signalling. *Nature* **467**, 1118-1122 (2010). https://doi.org/10.1038/nature09468

71 Takamatsu, H. & Kumanogoh, A. Diverse roles for semaphorin-plexin signaling in the immune system. *Trends in immunology* **33**, 127-135 (2012). https://doi.org/10.1016/j.it.2012.01.008

72 Li, Y. *et al.* Macrophages facilitate peripheral nerve regeneration by organizing regeneration tracks through Plexin-B2. *Genes Dev* **36**, 133-148 (2022). https://doi.org/10.1101/gad.349063.121

73 Paldy, E. *et al.* Semaphorin 4C Plexin-B2 signaling in peripheral sensory neurons is pronociceptive in a model of inflammatory pain. *Nature communications* **8**, 176 (2017). https://doi.org/10.1038/s41467-017-00341-w

74 Li, J., Liu, H. Q., Li, X. B., Yu, W. J. & Wang, T. Function of Adenosine 2A Receptor in High-Fat Diet-Induced Peripheral Neuropathy. *J Diabetes Res* **2020**, 7856503 (2020). https://doi.org/10.1155/2020/7856503

75 Kopan, R. & Ilagan, M. X. The canonical Notch signaling pathway: unfolding the activation mechanism. *Cell* **137**, 216-233 (2009). https://doi.org/10.1016/j.cell.2009.03.045

76 Zhang, Y., Lowe, S., Ding, A. Z. & Li, X. Notch-dependent binary fate choice regulates the Netrin pathway to control axon guidance of Drosophila visual projection neurons. *Cell Rep* **42**, 112143 (2023). https://doi.org/10.1016/j.celrep.2023.112143

77 Sullivan, J. M. *et al.* Dominant mutations of the Notch ligand Jagged1 cause peripheral neuropathy. *The Journal of clinical investigation* **130**, 1506-1512 (2020). https://doi.org/10.1172/jci128152

78 Wolfes, A. C. & Dean, C. The diversity of synaptotagmin isoforms. *Curr Opin Neurobiol* **63**, 198-209 (2020). https://doi.org/10.1016/j.conb.2020.04.006

79 Ullah, N., Maaiden, E. E., Uddin, M. S. & Ashraf, G. M. Synaptotagmin-1: A Multi-Functional Protein that Mediates Vesicle Docking, Priming, and Fusion. *Curr Protein Pept Sci* **22**, 470-478 (2021). https://doi.org/10.2174/1389203722666210325110231

80 Thiel, G. Synapsin I, synapsin II, and synaptophysin: marker proteins of synaptic vesicles. *Brain pathology* **3**, 87-95 (1993). https://doi.org/10.1111/j.1750-3639.1993.tb00729.x

81 Cesca, F., Baldelli, P., Valtorta, F. & Benfenati, F. The synapsins: key actors of synapse function and plasticity. *Progress in neurobiology* **91**, 313-348 (2010). https://doi.org/10.1016/j.pneurobio.2010.04.006

82 Park, D. *et al.* Cooperative function of synaptophysin and synapsin in the generation of synaptic vesicle-like clusters in non-neuronal cells. *Nature communications* **12**, 263 (2021). https://doi.org/10.1038/s41467-020-20462-z

83 Talagas, M. Anatomical contacts between sensory neurons and epidermal cells: an unrecognized anatomical network for neuro-immuno-cutaneous crosstalk. *Br J Dermatol* **188**, 176-185 (2023). https://doi.org/10.1093/bjd/ljac066

84 Vieira, W. F. *et al.* Anti-hyperalgesic effects of photobiomodulation therapy (904 nm) on streptozotocin-induced diabetic neuropathy imply MAPK pathway and calcium dynamics modulation. *Sci Rep* **12**, 16730 (2022). https://doi.org/10.1038/s41598-022-19947-2

85 Aghaee-Bakhtiari, S. H. *et al.* MAPK and JAK/STAT pathways targeted by miR-23a and miR-23b in prostate cancer: computational and in vitro approaches. *Tumour Biol* **36**, 4203-4212 (2015). https://doi.org/10.1007/s13277-015-3057-3

86 Perdas, E., Stawski, R., Nowak, D. & Zubrzycka, M. The Role of miRNA in Papillary Thyroid Cancer in the Context of miRNA Let-7 Family. *Int J Mol Sci* **17** (2016). https://doi.org/10.3390/ijms17060909

87 Wang, S. *et al.* MicroRNA-24 in Cancer: A Double Side Medal With Opposite Properties. *Front Oncol* **10**, 553714 (2020). https://doi.org/10.3389/fonc.2020.553714

88 Lin, Y. *et al.* miR-24-3p stimulates migration, invasion and proliferation of prostate cancer cells by targeting suppressor of cytokine signaling 6. *Int J Clin Exp Pathol* **11**, 1803-1810 (2018).

89 Xiang, Y. miR-24 in diabetes. *Oncotarget* **6**, 16816-16817 (2015). https://doi.org/10.18632/oncotarget.4795

90 George, D. S. *et al.* A subpopulation of peripheral sensory neurons expressing the Mas-related G Protein-Coupled Receptor d (Mrgprd) generates pain hypersensitivity in painful diabetic neuropathy. *bioRxiv*, 2022.2010.2027.514066 (2022). https://doi.org/10.1101/2022.10.27.514066

91 George, D. S. *et al.* The Mas-related G protein-coupled receptor d (Mrgprd) mediates pain hypersensitivity in painful diabetic neuropathy. *Pain* (2023). https://doi.org/10.1097/j.pain.0000000000003120

92 Asadi, J. *et al.* Enhanced imaging of lipid rich nanoparticles embedded in methylcellulose films for transmission electron microscopy using mixtures of heavy metals. *Micron* **99**, 40-48 (2017). https://doi.org/10.1016/j.micron.2017.03.019

93 Menichella, D. M. *et al.* Ganglioside GM3 synthase depletion reverses neuropathic pain and small fiber neuropathy in diet-induced diabetic mice. *Molecular pain* **12** (2016). https://doi.org/10.1177/1744806916666284

94 Eng, J. K., McCormack, A. L. & Yates, J. R. An approach to correlate tandem mass spectral data of peptides with amino acid sequences in a protein database. *J Am Soc Mass Spectrom* **5**, 976-989 (1994). https://doi.org/10.1016/1044-0305(94)80016-2

95 Xu, T. *et al.* ProLuCID: An improved SEQUEST-like algorithm with enhanced sensitivity and specificity. *J Proteomics* **129**, 16-24 (2015). https://doi.org/10.1016/j.jprot.2015.07.001

96 Cociorva, D., D, L. T. & Yates, J. R. Validation of tandem mass spectrometry database search results using DTASelect. *Curr Protoc Bioinformatics* **Chapter 13**, Unit 13.14 (2007). https://doi.org/10.1002/0471250953.bi1304s16

97 Tabb, D. L., McDonald, W. H. & Yates, J. R., 3rd. DTASelect and Contrast: tools for assembling and comparing protein identifications from shotgun proteomics. *J Proteome Res* **1**, 21-26 (2002). https://doi.org/10.1021/pr015504q

98 UniProt: a hub for protein information. *Nucleic Acids Res* **43**, D204-212 (2015). https://doi.org/10.1093/nar/gku989

99 Chen, Y. & Wang, X. miRDB: an online database for prediction of functional microRNA targets. *Nucleic Acids Res* **48**, D127-d131 (2020). https://doi.org/10.1093/nar/gkz757